Article ID: 1006-8775(2013) 03-0284-13

NUMERICAL SIMULATION OF CLOUD MICROPHYSICAL CHARACTERISTICS OF LANDFALL TYPHOON KROSA

HUA Cong (花　丛), LIU Qi-jun (刘奇俊)

(National Meteorological Center, Beijing 100081 China)

Abstract: In this study, the super typhoon KROSA (2007) was simulated using a mesoscale numerical model Global and Regional Assimilation and Prediction System (GRAPES) with a two-moment mixed-phase microphysics scheme. Local rainfall observations, radar and satellite data were also used to analyze the precipitation structure and microphysical features. It was shown that low-level jets and unstable temperature stratification provided this precipitation process with favorable weather condition. Heavy rainfall centers were located in the north and east part of KROSA with the maxima of 6-hourly total rainfall during the simulation more than 100 mm. The quantities of column solid water and column liquid water were generally equivalent, indicating the important role of ice phase in precipitation formation. Results of CloudSat showed that strong convection occurred in the eyewall around the cyclonic center. According to the simulation results, heavy precipitation in the northeast part of the typhoon was mainly triggered by convective clouds, accompanied by the strongest updraft under the melting level. In the southwest part of KROSA, precipitation intensity was rather homogeneous. The ascending center occurred in high-level cold clouds, favoring the formation and growth of ice particles.

Key words: typhoon heavy rainfall; KROSA; GRAPES model; two-moment mixed-phase microphysics scheme; cloud microphysics

CLC number: P444 **Document code:** A

1 INTRODUCTION

China is one of the countries in the world heavily influenced by landfall tropical cyclones (TCs). The annual mean direct economic losses caused by landfall TCs are 29 billion yuan (equivalent to about US$6.19 billion)[1]. Heavy rainfall brought by TCs is a major contributor to disasters. Significant progress has been made in research associated with typhoon storms in the past decade, such as the formation of spiral rainbands, the function of underlying surface, and the interactions between TCs and mesoscale systems[2-4]. Meanwhile, studies also pointed out that cloud microphysical processes have a significant impact on the intensity, structure and precipitation of TCs.

In recent years, cloud-resolving simulation with mesoscale numerical models with detailed cloud microphysical processes has become more and more attractive in TC research. It is suggested that cloud microphysical processes are critical to the realistic simulations of TC clouds and precipitation. Zhu and Zhang[5] found that the weakest and shallowest storm with little rainwater takes place without ice microphysics. Wang[6] reported that both evaporation of rain and melting of snow and graupel are responsible for the generation of downdrafts and rainbands. Franklin et al.[7] showed that rain rates in the inner core of the storm become higher with increasing speeds of graupel fall.

Super typhoon Krosa (2007) first appeared over the ocean east of Luzon in the Philippines at 0000 Coordinated Universal Time (UTC) 2 October 2007, and subsequently moved northwestward. At 1800 UTC 4 October, Krosa strengthened into a super typhoon with its central pressure down to 935 hPa. At 0730 UTC 7 October, Krosa made landfall at Xiaguan town located at the junction of Fujian and Zhejiang provinces, with a central pressure of 975 hPa. After that, Krosa weakened into a strong tropical storm and moved northeastward along the Zhejiang coastline. Krosa returned to the East China Sea at 0930 UTC 8 October and damped into a tropical depression at 1500 UTC 8 October.

Krosa was strong and stayed over the mainland of China for 26 hours, which was rarely seen in the same

Received 2012-04-24; **Revised** 2013-05-08; **Accepted** 2013-07-15
Foundation item: "Abnormal Changes and Mechanism Study Before and After Typhoon Landing" (2009CB421500) from the National Key Basic Research Program (973 Program)
Biography: HUA Cong, M.S., primarily undertaking research on cloud model and cloud microphysics.
Corresponding author: HUA Cong, e-mail: floweronly@163.com

period of history. Its long-term effects brought heavy rainfall to north Fujian and most of Zhejiang province. There have been studies[8, 9] considering the mesoscale cloud clusters in spiral cloud bands as the main reason for precipitation during early landfall. Spiral cloud bands provided favorable moisture conditions to the heavy rainfall. An inverted trough resulted in the coupling of upper divergence and lower convergence, enhancing precipitation in the north of Krosa. Cold air invaded into the cyclone to increase atmospheric baroclinic instability, assisting the maintenance of heavy rainfall.

In this study, super typhoon Krosa (2007) was simulated using a mesoscale numerical model, Global and Regional Assimilation and Prediction System (GRAPES), which is independently developed in China. Local rainfall observations, radar and satellite data were also used to analyze the precipitation structure and microphysical features.

2 THE MICROPHYSICAL SCHEME

GRAPES[10] is a numerical forecasting model designed for both scientific research and operation. Its physics schemes, which are used to describe the atmosphere and underlying surface processes, include radiation transfer, boundary layer processes, sub-grid moist convection, grid-scale cloud and precipitation processes, surface-layer physics process and sub-grid scale terrain gravity wave drag. Here we used the GRAPES-Meso model with a two-moment mixed-phase microphysics scheme[11]. The continuity equation for hydrometeor mixing ratios, hydrometeor number concentration ratios and spectrum broaden functions in this scheme is written as:

$$\frac{\partial F_x(m)}{\partial t}=-\nabla\cdot\left(\vec{U}F_x(m)\right)+\nabla\cdot\left(K_m\nabla\cdot F_x(m)\right)+\frac{\partial}{\partial z}\left(U_xF_x(m)\right)+\frac{\delta F_x(m)}{\delta t}$$

where $F_x(m)$ stands for hydrometeor mixing ratios *of* Q_v, Q_c, Q_r, Q_i, Q_s and Q_g, hydrometeor number concentration ratios N_r, N_i, N_s, N_g, ice spectrum broaden function F_i and snow spectrum broaden function F_s. The right-hand-side terms of the equation are advection transport, turbulent diffusion, sedimentation and cloud microphysical sources and sinks, respectively. 29 kinds of microphysical processes are included in the scheme (Figure 1), such as condensation or evaporation of cloud droplets and raindrops, deposition or sublimation of ice crystals, snow crystals and graupel, automatic conversion of cloud droplets to raindrops, ice crystals to snow crystals, ice crystals to graupel, snow crystals to graupel; collection of cloud droplets and raindrops, cloud droplets and ice crystals, cloud droplets and graupel, ice crystals and ice crystals, rain drops and ice crystals, raindrops and snow crystals, raindrops and raindrops, ice crystals and graupel, ice crystals and snow crystals, snow crystals and graupel, snow crystals and snow crystals; nucleation of ice crystals; multiplication of ice crystals; melting of ice crystals, snow crystals and graupel; congelation of raindrops and cloud droplets, et al.

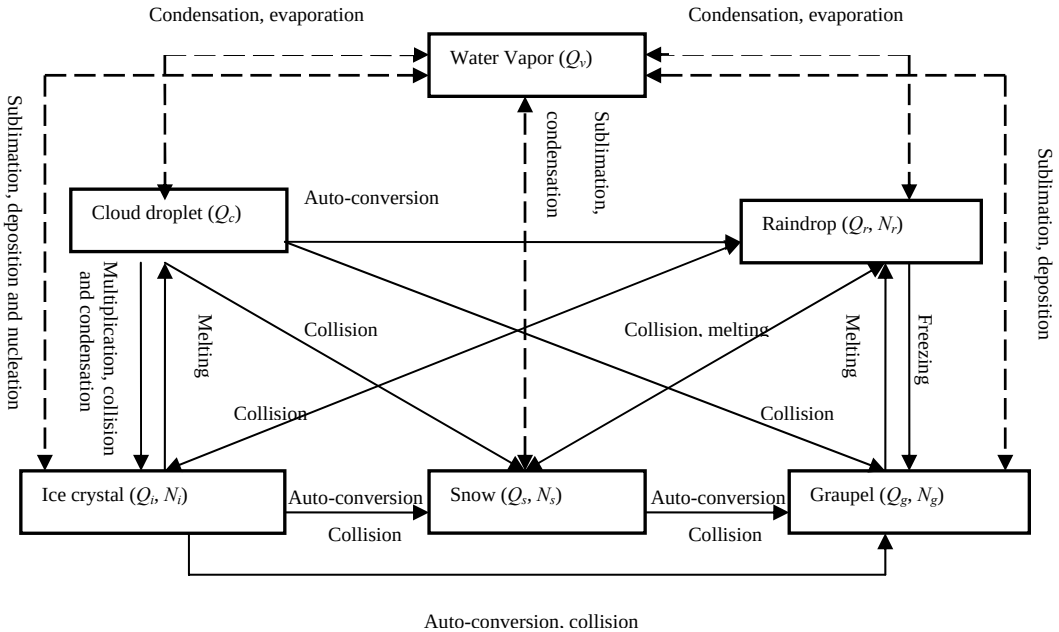

Figure 1. Microphysics processes in the two-moment mixed-phase scheme.

Except for the mutual transformation of the microphysics, the scheme also took traction on the dynamic field and the latent heat release into consideration. The temperature equation is given by

$$\frac{\partial T}{\partial t} = -\nabla \cdot \left(\vec{U}\, T \right) + \nabla \cdot \left(K \nabla \cdot T \right) + \frac{\partial}{\partial z}\left(UT \right) + \frac{\delta T}{\delta t}$$

where $\frac{\delta T}{\delta t}$ is latent heat induced by phase change.

3 EXPERIMENT DESIGN

The physics options adopted in the simulation are listed in Table 1, and the two-moment mixed-phase microphysics scheme introduced above is chosen as the microphysics scheme. A triply nested, one-way mode is used in the simulation, indicating the inner grid is run with the initial and boundary conditions provided by outer coarse grids. The T213 forecast field incorporated with a bogus vortex is adopted as the initial field. All three nested domains have the same initial physical quantities, including horizontal wind speed u and v, temperature t, geopotential height h, water vapor content Q_v, sea level pressure p_s and sea level temperature t_s. Figure 2 shows the model domains. Domain 3, with a horizontal resolution of 3.3 km, covers the five provinces in East China severely affected by Krosa, and only an explicit microphysical scheme is applied. See Table 2 for more details.

Table 1. Summary of the physics scheme.

Physics	Scheme
Microphysics	Ice scheme
Longwave radiation physics	RRTM scheme
Shortwave radiation physics	Dudhia scheme
Surface-layer physics	Monin-Obukhov scheme
Land-surface physics	Thermal diffusion scheme
Boundary-layer physics	MRF scheme
Cumulus physics	Kain-Fritsch (new Eta) scheme (only for domain 1&2)

Table 2. Summary of the experiment design.

Domain	Simulation time	Resolution /km	Time step/s	Vertical levels
1	1200 UTC October 6 to 1200 UTC October 8, 2007	17.6	60	17
2	0000 UCT October 7 to 1200 October 8, 2007	6.0	30	17
3	0600 UCT October 7 to 0600 October 8, 2007	3.3	10	22

4 MODEL VERIFICATION

4.1 *Track and intensity*

Figure 3a compares the model-simulated track of Krosa with the 6-hourly best track from Shanghai Typhoon Institute, China Meteorological Administration (STI-CMA), using results from the largest-scale domain with a horizontal resolution of 17.6 km. In general, the GRAPES simulates Krosa's track well before its landing. After landing Taiwan Island, the storm moves northwestward. The observed and simulated storm centers are closely located within 100 km until 0000 UTC 8 October (Figure 3b). However, the simulated track begins to deviate from the observation after that moment. A possible reason is that the simulated storm first stagnates near the landing site and then moves southeastward into the ocean, which is different from the observed one.

Figure 3c shows that the observed storm intensity decreases evidently prior to landfall, with the central pressure increasing at a rate of about 2 hPa h^{-1} from 1200 UTC 6 October to 0600 UTC 7 October. Krosa experiences continuous weakening while moving inland, with a central pressure of 1006 hPa at 1200 UTC 8 October. Even though the simulated storm intensity is weaker than that of the estimated best-track at first, the central pressure increases continuously hereafter. At the end of the experiment, the simulated storm is stronger than the observation. Although there is obvious deviation at the beginning, model results and observed intensity are much alike during the heavy precipitation period. Therefore, the

model results are applicable.

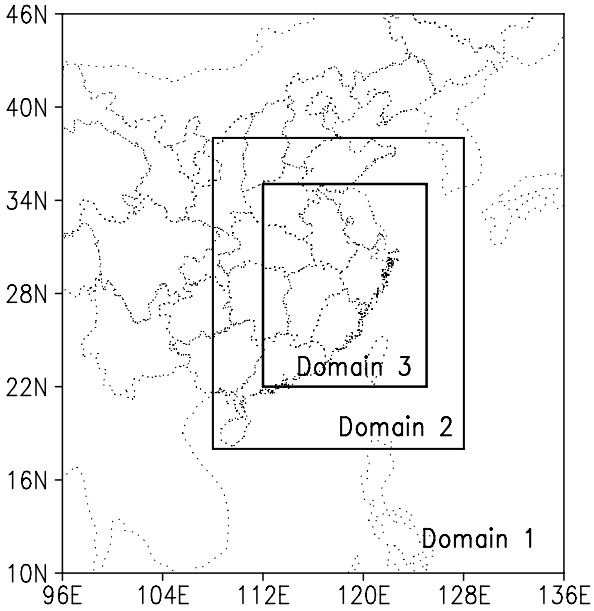

Figure 2. The nested model domains.

4.2 *Horizontal velocity structure*

From 1200 UTC 7 and 0000 UTC 8 October, the landed Krosa brought a wide range of precipitation to East China. Considering the comparable track and intensity with the observation at that time, these two moments are selected to analyze the dynamical structure of Krosa. Since the dynamic and thermodynamic structure of Domain 1 and Domain 3 are similar (figure omitted), the results from Domain 1 are used to examine the precipitation structure of Krosa in a wider range. The storm center stays at 26.8 °N, 120.1 °E on 1200 UTC 7 October. Figure 4a reflects that the horizontal velocity shows an asymmetric structure clearly with the eye wall stretching up to 350 hPa. To the south of the eye, the maximum wind speed of 21 m/s appears at the mid-level of 600 hPa, 1.5 latitudes away from the storm center. To the north of the eye, the same wind speed exists at the low-level of 920 hPa, 4 latitudes away from the storm center. A broad low-level jet, which acts as a major water vapor channel, has been reported by many researchers[7, 12]. With the weakening of Krosa, the south wind core decreases since 0000 UTC 8 October, whereas the north center strengthens over 27 m/s. Meanwhile, surface precipitation is strengthened as well.

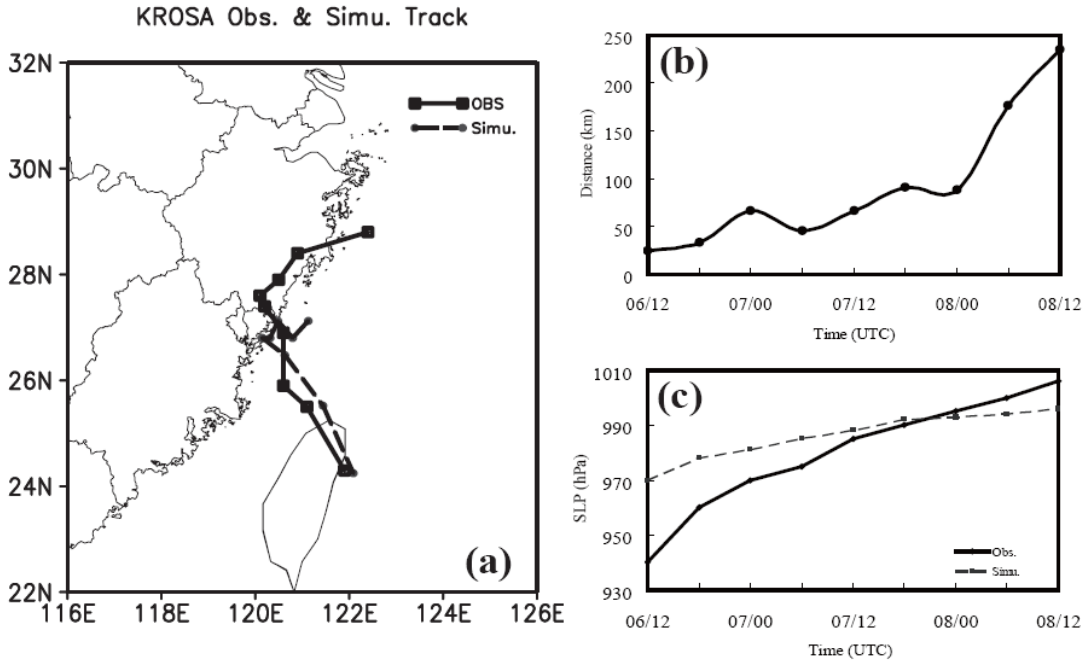

Figure 3. Comparison of (a) the 6-hourly STI-CMA best track and the simulated track of Typhoon Krosa; (b) the time series of center distance (units: km) and (c) the minimum sea level pressure (units: hPa) during the period of 1200 UTC 6 October to 1200 UTC 8 October.

4.3 *Thermodynamic structure*

At 1200 UTC 7 October, the storm shows significant warm core structure with two warm centers of 356 K located at 300 hPa and 800 hPa, respectively (Figure 5a). Equivalent potential temperature (θ_e) decreases with increasing altitude between 600 hPa and 900 hPa. According to the potential instability criterion, the atmosphere becomes convectively instable while $\frac{\partial \theta_e}{\partial z} < 0$. A wide range of strong convection forms with the ascending flow. Low-level convergence around the eye, coupled with unstable

temperature stratification, favors the occurrence of heavy precipitation. At 0000 UTC 8 October, the low-level warm core splits into two parts, and its center decreases to 354 K. Equipotential isotherms below 900 hPa are nearly vertical between 31 and 33 °N. Strong winds in the low-level jet bring air upward and lead to a neutral stratification relatively uniform in temperature and water vapor distribution.

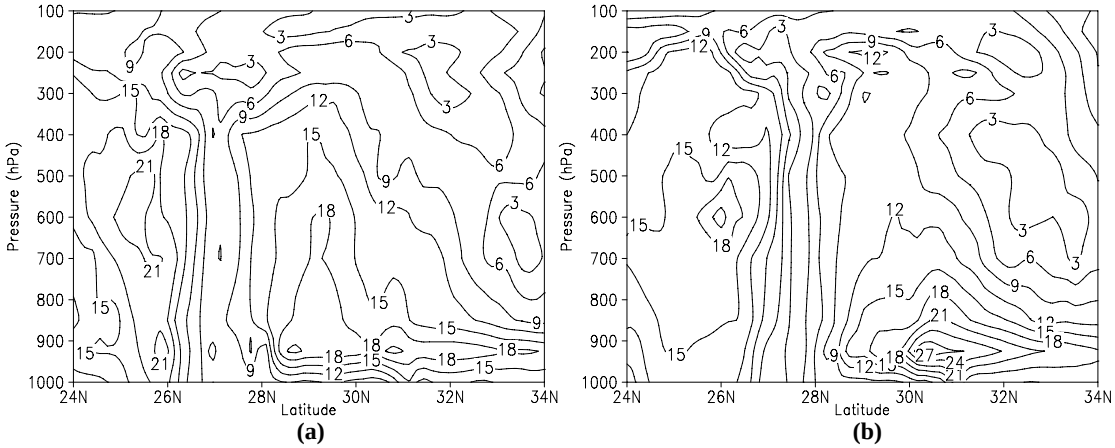

Figure 4. Pressure-latitude cross sections of horizontal velocity distribution through the Krosa's center (units: m/s) at (a) 1200 UTC 7 October and (b) 0000 UTC 8 October, respectively.

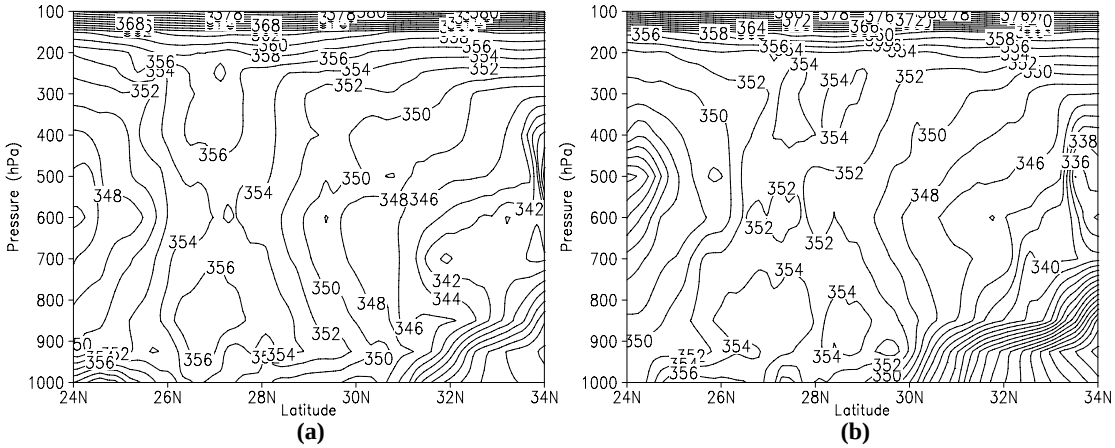

Figure 5. Pressure-latitude cross sections of equivalent potential temperature through the storm center (units: *K*) at (a) 1200 UTC 7 October and (b) 0000 UTC 8 October, respectively.

4.4 *Accumulated rainfall*

Figure 6 compares the simulated 6-h accumulated rainfall from 0600 UTC 7 October to 0600 UTC 8 October with the observed one. The observed data is from the observations of intensive rain gauges while the simulated rainfall is from Domain 3 results.

From 0600 UTC to 1200 UTC 7 October, Krosa made its landfall and moved northwestward. Krosa's circulation (southeasterly and easterly) gave rise to a rainfall amount exceeding 100 mm over the eastern Zhejiang province (Figure 6a). When Krosa moved northeastward, the precipitation divided into two centers. One is located at the junction of Jiangsu, Zhejiang and Anhui provinces, and the other situated over the southeastern Zhejiang province (Figure 6b). It is evident that the model captures the rainfall distribution and some local rainfall maxima (Figure 6e and 6f). Subsequently, Krosa moved further inland, and the two precipitation centers began to merge together. A rainfall maximum of 100 mm appeared over the northeastern Zhejiang province (Figure 6c). The simulated rainfall center is located over the south of Jiangxi province, which is a little more northwestward from the observed (Figure 6g). Krosa moved northward and weakened continuously since 0000 UTC 8 October, accompanied by the reduced coverage and intensity of rainfall in observation (Figure 6d). However, the simulated storm retains its intensity and position at the same time. As a result, the simulated rainfall covers the same area as the previous 6 hours, and the rainfall intensity is only slightly decreased (Figure 6h).

Overall, the model could simulate the general characteristics of the measured rainfall distribution and intensity, except that the observed rainfall that exceeds 10 mm is located to the north of the storm center, while the simulation produces more complete spiral rainbands. Part of this difference appears to result from the lack of rain gauge stations at sea, so

that the rain belts on the north and east sides of the storm cannot be observed. Moreover, the simulated storm is a bit more southward from the observation, thus the convergence in the south tends to be stronger, resulting in heavier local rainfall.

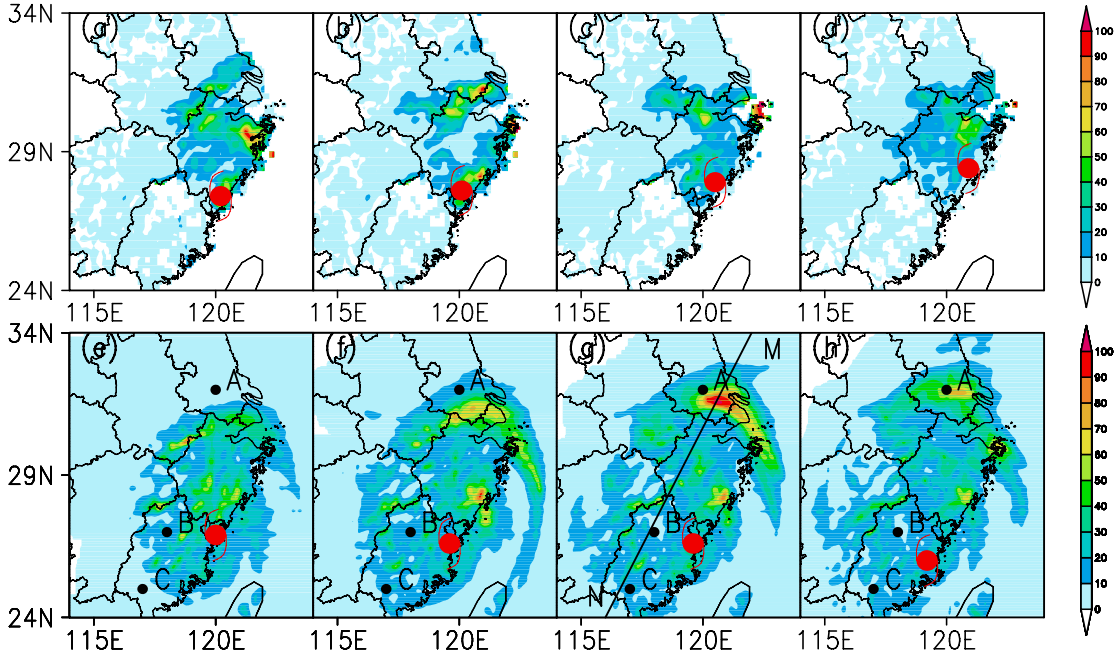

Figure 6. Horizontal distribution of the 6-h accumulated rainfall (units: mm) from the observations (upper panels) and 3.3-km grid simulations ((bottom panels) from 0600 UTC 7 October to 0600 UTC 8 October. The typhoon symbol denotes the surface storm center at the last hour in each time period. (a) and (e): 0600 and 1200 UTC 7 October; (b) and (f): 1200 and 1800 UTC 7 October; (c) and (g): 1800 UTC 7 and 0000 UTC 8 October; (d) and (h): 0000 and 0600 UTC 8 October.

4.5 *Horizontal reflectivity*

The composite of observed radar reflectivity at 1200 UTC 7 October showed asymmetry with weaker intensity in the southwest of the storm, which was caused by lower content of water vapor (Figure 7a). Severe convection was found in the east and north of the storm. Here a lump-like echo in the east side of the eye was greater than 45 dBZ. There were two obvious echo bands on the north side of the storm. The inner one of 55 dBZ was relatively greater than the outer one with the maximum being about 40 dBZ. The model well reproduces the stripe-like echo over the southern Zhejiang province (Figure 7b). Note that in the model the two echo bands merge together with a weaker reflectivity of about 45 dBZ. As shown in Figure 7c, the storm moved a little northward and its pattern gradually evolved into a comma shape at 0000 UTC 8 October. At that time, the reflectivity was significantly reduced, and the echo at the junction of Jiangsu and Zhejiang provinces and the neighboring sea had maximum intensity at about 50 dBZ. The simulation covers almost the same area as the observation but with weaker intensity at about 45 dBZ (Figure 7d).

4.6 *Column water content*

For further understanding the mechanisms and distribution of this precipitation, liquid and solid water content are integrated respectively. Here the liquid water content only includes cloud water (Q_c), while the solid one contains ice (Q_i), snow (Q_s) and graupel (Q_g).

As seen in Figure 8, hydrometeors are spirally distributed around the storm center. The value of integral cloud water content is 0.4 to 1.6 kg/m^2 on 1200 UTC 7 October. Random maxima of cloud water appear over southern Anhui and the junction of Jiangxi and Fujian provinces. The integral cloud water tends to decrease on 0000 UTC 8 October, with nearly constant water content. The locations of liquid water core and surface rainfall center are superimposed in general (see Figure 6e).

Solid water covers less area than liquid water does, but their spatial distribution is somewhat different. Column solid water mostly concentrates on the south side of the storm center with a maximum value of over 1.9 kg/m^2 at 1200 UTC 7 October. The distribution indicates that the ice particles grow fully under strong convection on the south side. On the north side of the storm, solid water is mainly at the junction of Jiangsu and Zhejiang provinces with a value of 0.4 to 0.8 kg/m^2. 12 hours later, solid water content increases on the north side of Krosa. The surface precipitation over this area increases significantly as well (Figure 6g). It can be speculated that the ice-phase process plays an important role in the precipitation of Jiangsu and Zhejiang provinces.

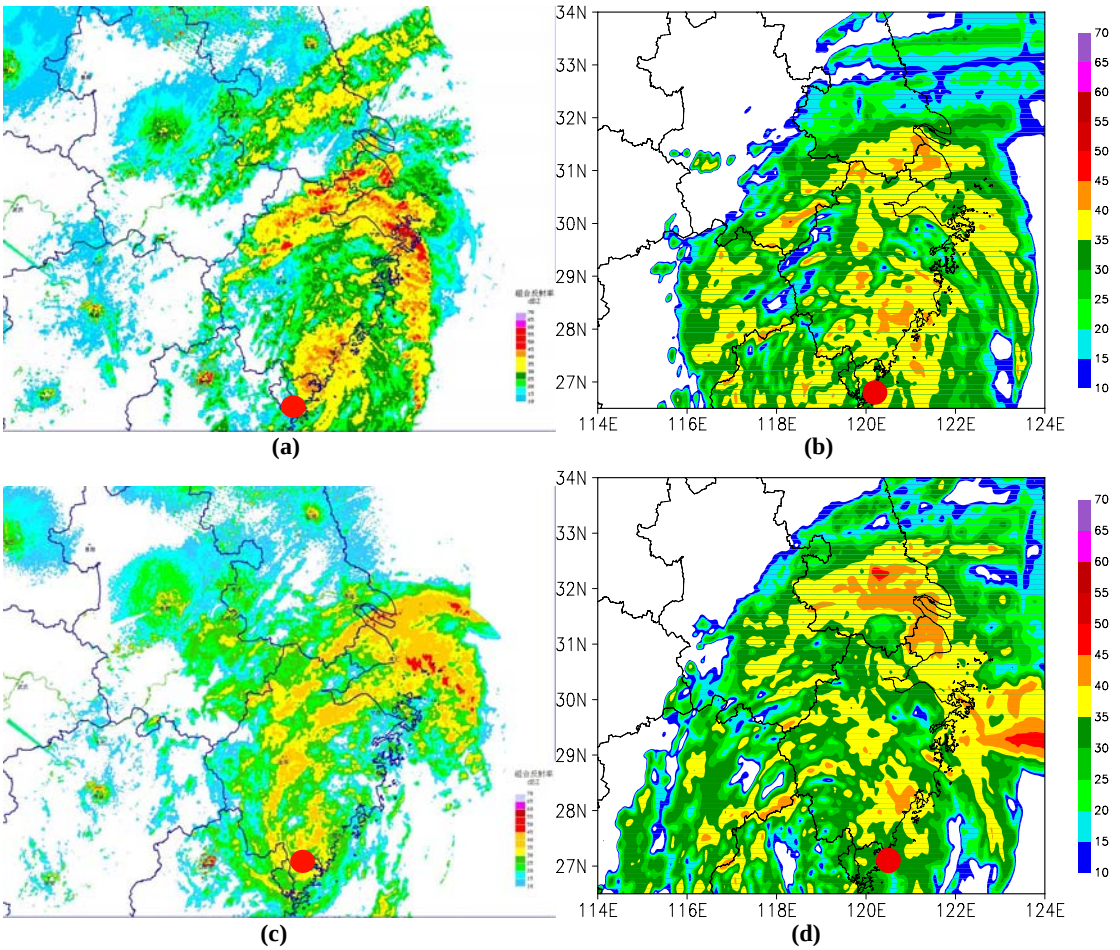

Figure 7. Radar reflectivity composites (a and c) and simulations (b and d) at 1200 UTC 7 October (a and b) and 0000 UTC 8 October (c and d, units: dBZ). The red dot indicates the surface storm center.

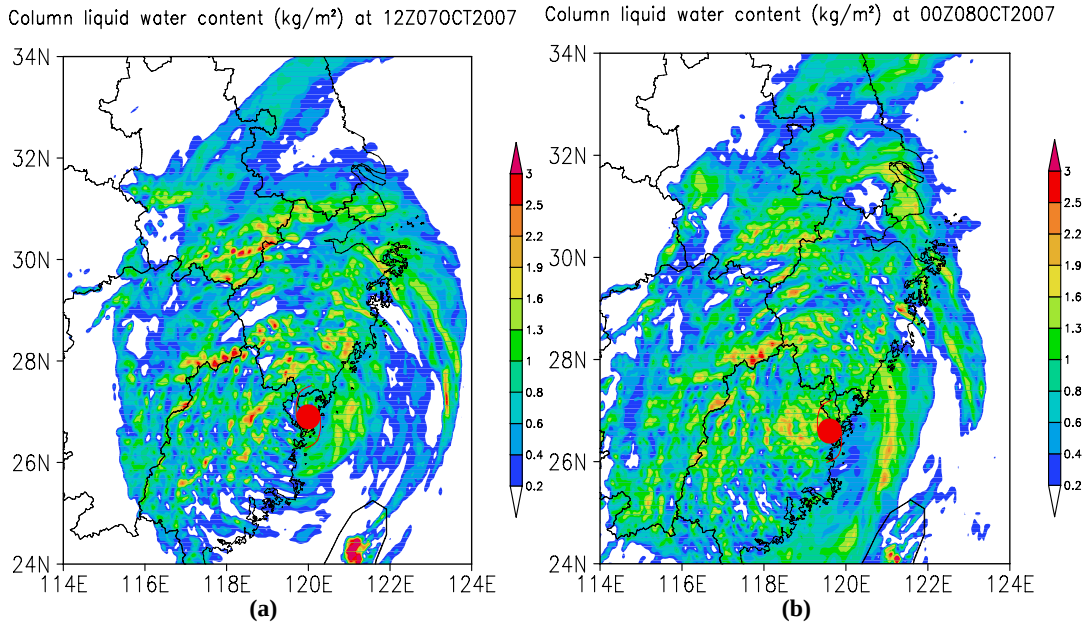

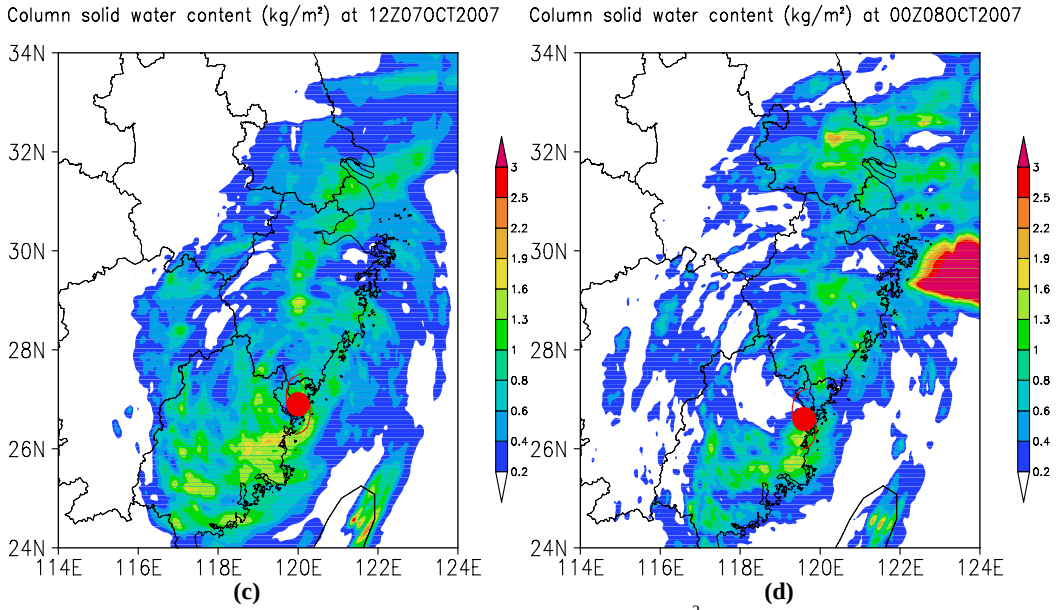

Figure 8. Column liquid water content and column solid water content (units: kg/m^2) at (a, c) 1200 UTC 7 October and (b, d) 0000 UTC 8 October. The typhoon symbol denotes the surface storm center.

4.7 *Cloud top temperature*

Cloud top temperature is an important parameter indicating the cloud system development. A more robust cloud system is consistent with a lower temperature of the cloud top. The model results are compared with the observation collected by Moderate Resolution Imaging Spectroradiometer (MODIS), which is flying onboard the Earth Observing System Terra and Aqua polar-orbiting satellite platforms. Model results from Domain 2 are used in order to reflect a wider range of cloud distribution. The lowest grid temperature is chosen as the simulated temperature of cloud top where the sum of cloud (Q_c), rain (Q_r), ice (Q_i), snow (Q_s) and graupel (Q_g) is greater than 1×10^{-6} kg/kg. The MODIS cloud products MOD06_L2 (observed by Terra) and MYD06_L2 (observed by Aqua) at 1-km pixel resolution are adopted.

Figure 9a shows that when Krosa was about to make landfall at 0510 UTC 7 October, its northern cloud band had already affected the southeast coast of China. The lowest value of cloud top temperature was over northeastern Zhejiang province with a minimum less than 200 K, according to the MODIS product. It can be deduced that the cloud at this area extended to higher altitude with adequate supply of water vapor. Cloud systems over the eye were relatively shallow with a cloud top temperature over 250 K. The model results have a similar distribution with the observed one, but the value is lower (Figure 9d). The lowest simulated temperature is in the south of the eye wall.

At 1435 UTC 7 October, Krosa had weakened after landfall and its observed lowest cloud top temperature rose to over 200 K (Figure 9b). Two strong convective clouds were formed over Hangzhou Bay and southeastern Zhejiang province, respectively. The model overestimated these two cloud clusters with lowest cloud top temperature less than 200 K (Figure 9e). In the model results, at this time the storm is gradually scattered in structure with the spiral cloud band tending to vanish.

At 0240 UTC 8 October, the MODIS data showed that the cloud top height was further declined (Figure 9c). Convective clouds in front of the storm had completely moved onto the ocean. Cloud top temperature over the eye had risen up to 260 K. Figure 9f shows that the simulated storm is more southward from the observation. Similar to the satellite results, the simulated cloud top temperature over the storm center is also above 260 K. Convective clouds distribute around the storm center where the surface heavy rainfall occurs.

In brief, the model simulates the cloud bands structure and its variation correctly. Convective clouds around the storm center correspond to the surface heavy precipitation center. Though being higher on the south side of the storm, the simulated cloud top temperature is generally lower than that in the MODIS product.

4.8 *Comparison with CloudSat*

The CloudSat, launched in 2004, has a cloud profile radar (CPR) onboard. The CPR can detect the internal structure of cloud and precipitation[13]. It provides products to understand the real characteristics of cloud structure and cloud processes, thereby improving the awareness and forecast ability with regards to synoptic systems and cloud microphysics[14, 15].

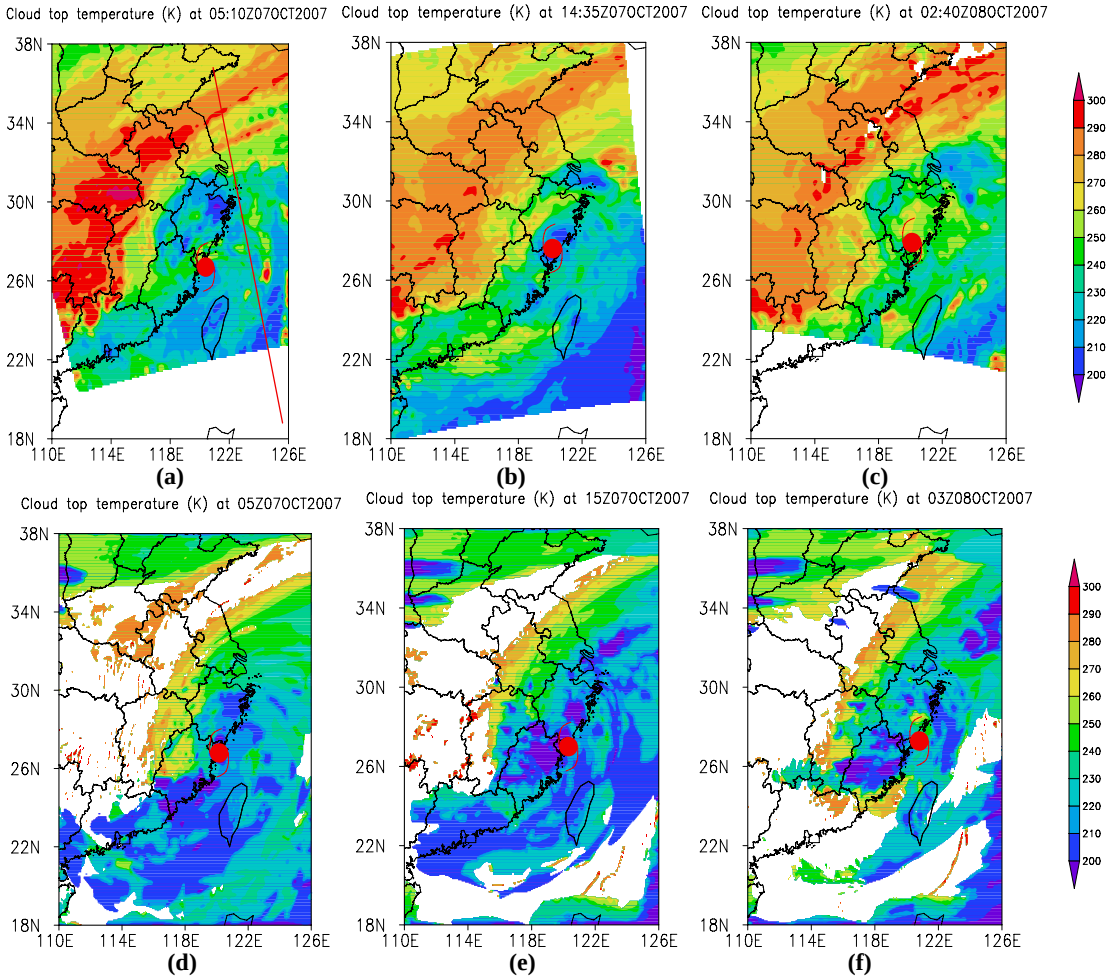

Figure 9. MODIS-retrieved (a, b, c) and corresponding simulated (d, e, f) cloud top temperatures (units: *K*). The typhoon symbol denotes the surface storm center.

CloudSat scanned through the east part of Krosa center at about 0500 UTC 7 October (Figure 10a). Satellite products, including 2B-GEOPROF, 2B-CWC-RO and ancillary product ECMWF-AUX, all with a vertical resolution of 240 m, are used in this section. Considering the coverage of CloudSat, model results from Domain 2 are used to carry out the comparison.

The center of the storm was located on 120.6 °E, 26.7 °N at 0500 UTC 7 October with a central pressure of 970 hPa. Figure 10a shows the vertical structure of reflectivity from CPR. It can be seen that cloud top on the east side of storm center reached up to 200 hPa, with a lower cloud top of 300 hPa near the outer band. Most of strong convection formed in the eyewall. Furthermore, the cloud extended around in the upper level. Simulated reflectivity represents similar distribution and intensity as that observed by the satellite (Figure 10b).

Figure 10c shows the ice water distribution detected by CloudSat. Ice water around the storm center was located above the 0°C isotherm, manifesting a larger content and wider expansion than that of the outer area. It reached a maximum of 0.40 g/m^3 between 300 and 400 hPa. Ice water expanded more to the south but shrunk sharply from the north of the storm center, with only little particles existing in the middle layer. The simulated ice water is distributed similarly as that in the CloudSat products, but with a lower maximum of 0.30 g/m^3 (Figure 10d). It can be deduced that during the Krosa landfall, relatively high content of ice water was in the storm with wide expansion. Consequently, the ice-phase process is also important in the occurrence of surface precipitation.

4.9 *Precipitation features in different positions of Krosa*

Precipitation resulting from Krosa is featured by the long duration and wide coverage. Since the TC is a complex multi-scale system, efforts are worth taking to investigate the mechanism about precipitation. For further understanding the structure and formation of rainfall in different positions, three typical points are selected to analyze their microphysical characteristics.

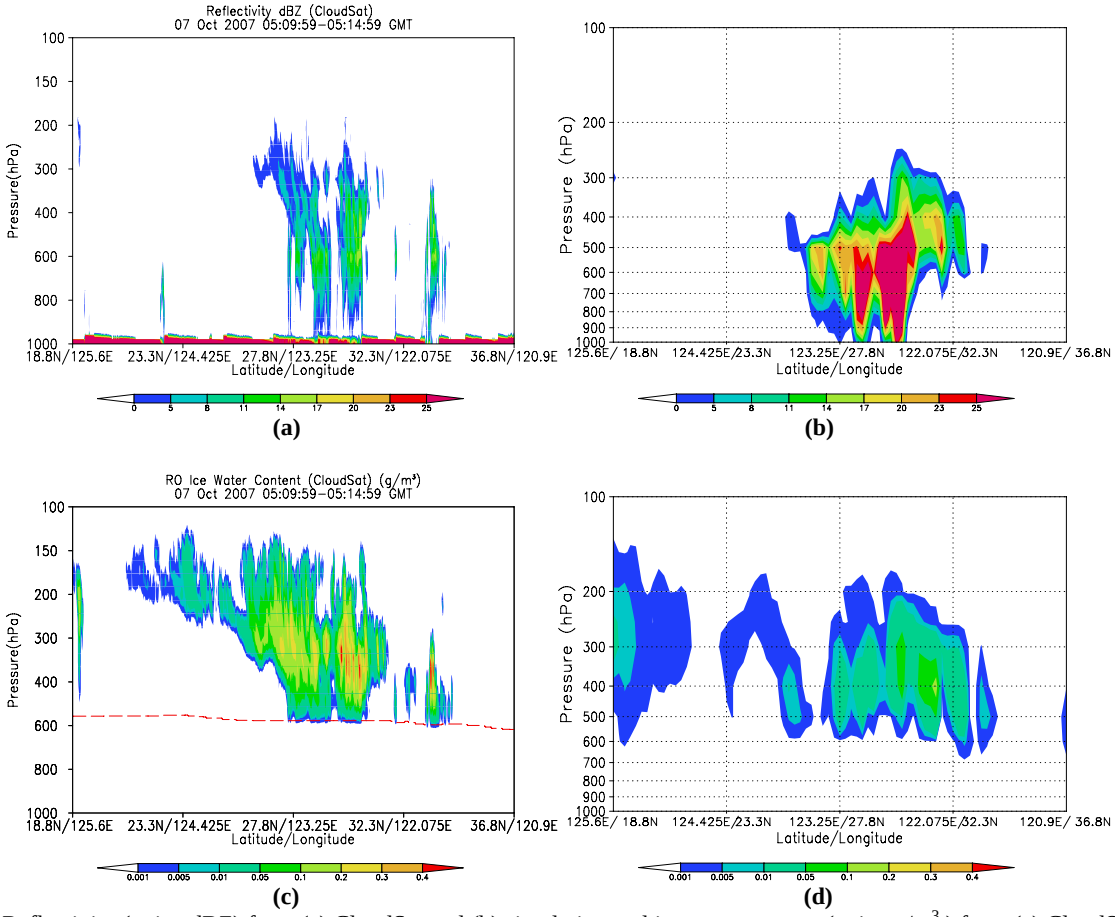

Figure 10. Reflectivity (units: dBZ) from (a) CloudSat and (b) simulation and ice water content (units: g/m^3) from (c) CloudSat and (d) simulation. The red dash line denotes the 0°C isotherm.

4.9.1 VERTICAL STRUCTURE

Take the precipitation at 0000 UTC 8 October for example. Seen from the 1-h accumulated rainfall (Figure 11a), precipitation around the storm center was asymmetrically distributed. And the rain belt was primarily in a northeast-southwest direction. Rainfall centered on the northeast side of the storm and covered southern Jiangsu province and Hangzhou Bay with a maximum of 18 mm. There was small rainfall (2 to 12 mm per hour) on the southwest side of the storm. Here detailed analysis will be done on Point A of the heavy precipitation area, Point B of the storm eye and Point C for the weaker precipitation area.

At Point A (Figure 11b), the atmosphere below 500 hPa was weakly supersaturated with a relative humidity of 101%. There was plenty of graupel between 300 and 600 hPa, with the maximum at 0.62 g/kg at 500 hPa. Considering little snow and ice in the upper level, the graupel mainly grew from the collision between cloud droplets and ice and snow. The maximum of cloud water content was 0.65 g/kg at 500 to 600 hPa. Rain water content has a peak of 0.62 g/kg around 650 hPa. According to the analysis above, the precipitation at Point A primarily came from the melting of graupels, the auto-conversion from cloud droplets to rain, and the collision between rainwater and cloud droplets.

At Point B, which is located at the eye (Figure 11c), the middle and lower atmosphere between 500 and 850 hPa was in saturation or weak supersaturation. The distribution of cloud water was similar to that of Point A but with a lower maximum of 0.58 g/kg. Rain water content remained almost constant from the surface to 650 hPa. Downdraft was prevalent in the cyclone center, against the formation of large ice particles. As a result, the graupel content was lower than 0.10 g/kg.

Snow water content was evidently higher at Point C than that of Points A and B (Figure 11d). Due to the plentiful snow, relative humidity reached its peak around 220 hPa. Most of graupel was produced by collision between snow and supercold cloud water, and the maximum of graupel was 0.3 g/kg. Therefore, cold cloud precipitation was very important at this point. Auto-conversion of cloud and water vapor, collision between raindrops and cloud droplets and melting of snow and graupel were the major source of precipitation at Point C.

To sum up, no matter how much surface rainfall is, although the atmosphere below 500 hPa is all saturated or weakly supersaturated in different

position of the storm, the precipitation distribution is not similar. Deep convection in the northeast mainly comes from melting of graupel, auto-conversion of cloud to rain, and collision of raindrops to cloud droplets. While precipitation in the southwest is relatively uniform, and the melting of snow plays an important role in the stratiform rainfall region.

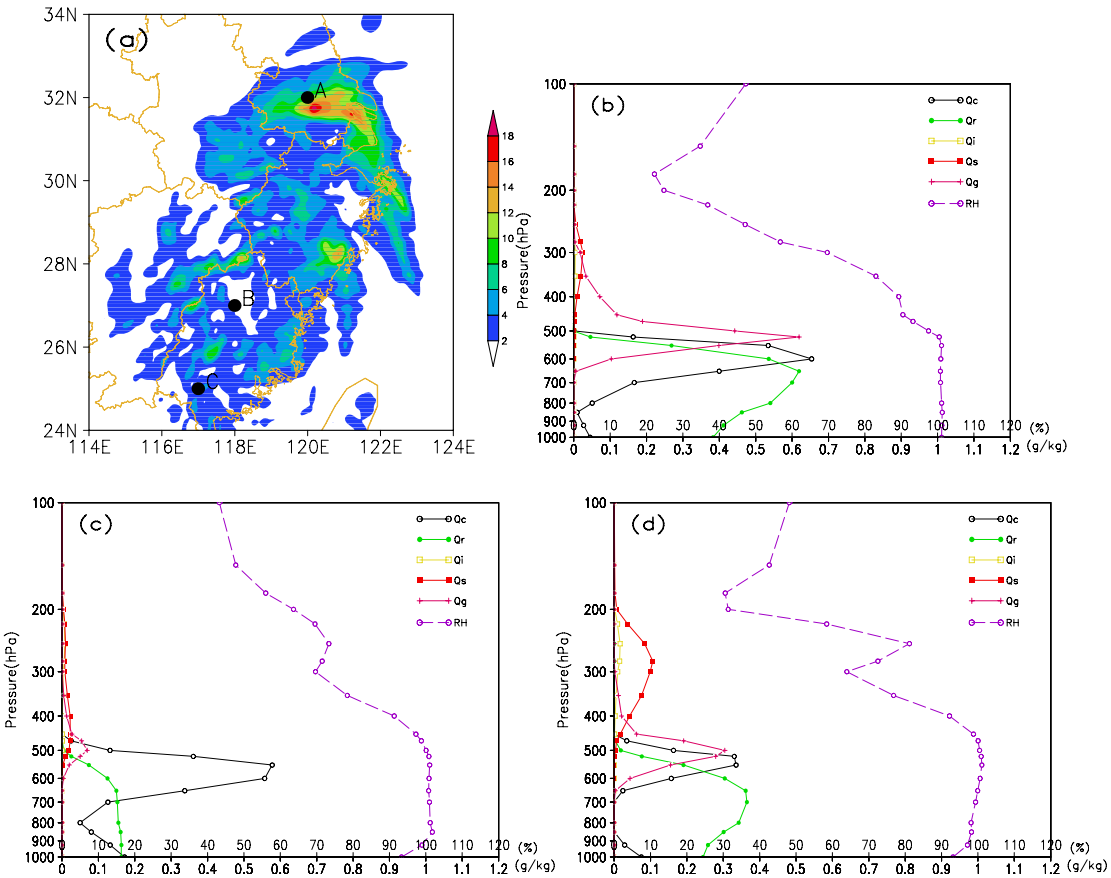

Figure 11. (a) 1-h accumulated rainfall (units: mm), cross sections of hydrometeors (units: g/kg) and relative humidity (units: %) at (b) Point A, (c) Point B and (d) Point C at 0000 UTC 8 October.

4.9.2 TOTAL WATER CONTENT AND VERTICAL MOTION

In the continuous process of a typhoon, water content and distribution are constantly changing. Combined with the vertical wind field, Points A, B and C are still used to further examine the features of water content and vertical motion varying from 0600 UTC 7 October to 0600 UTC 8 October. Figures 6e to 6h show the surface precipitation in this period.

Figure 12a shows that high-value water content concentrates below the 0℃ isotherm at Point A. Cold areas above the freezing level had little water and cloud top generally stays at 250 hPa. At the beginning of Krosa's landfall, water content was lower than 0.60 g/kg, and the vertical wind field was weak. As Krosa was going northward, water content gradually increased since 1800 UTC 7 October. In the following 12 hours, the central value of water content exceeded 1.0 g/kg, with the big value area stretching to the low level. Thus the vertical wind was strengthened with increased water content at low levels, reaching a maximum speed of 0.30 m/s. This shows that the formation of heavy precipitation is supported by strong convection.

Point B had been near the storm center since 1200 UTC 7 October, so that the sinking motion dominated all levels of the atmosphere (Figure 12b). Three descending cores were found at 210 hPa and 800 hPa at 1200 UTC 7 October and at 800 hPa at 1600 UTC 7 October, respectively, with a maximum of –0.25 m/s. Most hydrometeors concentrated under the freezing level. The maxima of total water content were between 0.6 and 0.9 g/kg since 1200 UTC 7 October. Because there was little rain in the eye, a low-value area of 0.10 to 0.20 g/kg appeared at 700 to 900 hPa from 1300 UTC 7 October to 0000 UTC 8 October. Compared with Point A, the cloud top was higher at Point B, exceeding 200 hPa most of the time.

The ascending motion was prevalent at Point C which was on the south side of the storm, with cloud top reaching 120 hPa. In the upper level, the centers of ascending motion and water content were superimposed, and the central speed was 0.30 m/s. However, in the middle and lower level, the center of ascending motion did not agree with that of water

content. Actually, the weak descending took place in the center of water content. On the whole, hydrometeor content was distributed symmetrically along the 0°C isotherm, which indicates that the hydrometeor in the cold zone accounts for a large proportion of total water content with a significant contribution to the precipitation.

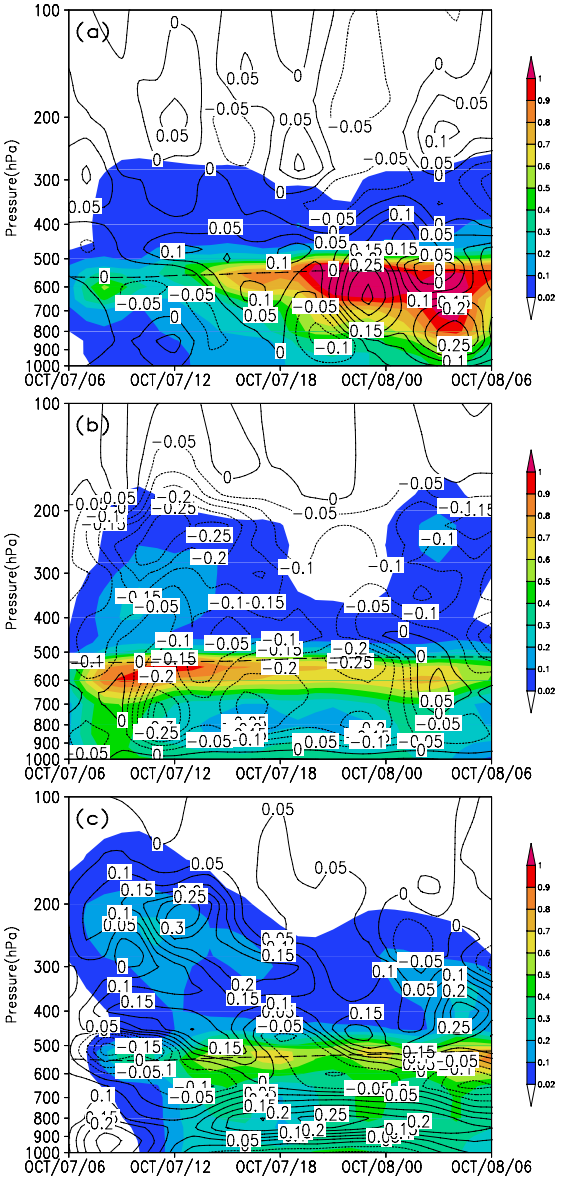

Figure 12. Time series of total water content (units: g/kg) and vertical motion (units: m/s) at (a) Point A, (b) Point B and (c) Point C from 0600 UTC 7 October to 0600 UTC 8 October. Shading: total water content; solid line: updraft; dotted line: downdraft; dashed line: 0 °C isotherm.

In summary, downdraft is popular in the storm center, and the distribution of hydrometeors in the outer cloud bands is closely related with the ascending motion. In the north part of the cloud band, which is Point A, the strongest updraft is found in a warm area below the freezing level, necessary for the formation of abundant precipitation particles. In contrast to that, in the south part of the storm, which is Point C, the strongest updraft is in the upper cold cloud and provides a favorable condition for the ice particles.

5 CONCLUSIONS

The super typhoon Krosa (2007) was simulated using the mesoscale numerical model GRAPES incorporated by a two-moment mixed-phase microphysics scheme. Local rainfall observations, radar and satellite products were also adopted to analyze the precipitation structure and microphysical features prior to and after the landfall of the storm. The major points to be noted are as follows.

(1) Overall, the low-level jet provides the north side of the storm center with moisture, the condition that leads to heavy precipitation together with favorable convergence. The southern cloud bands extend to higher levels with few ice particles fully grown. However, the water vapor content is not as abundant as that in the north cloud bands, resulting in relatively weak surface precipitation.

(2) The model well simulates the distribution, intensity and developing process of the precipitation. Both the observed and the simulated 6-h rainfall exceed 100 mm. Strong convection is mainly found in the north and east part of the cloud bands, with a maximum reflectivity of 55 dBZ.

(3) Column solid water content is comparable with column liquid water content, but with different spatial distribution. The liquid water core is superimposed on the surface rainfall center, while the solid water core changes with the development of the cloud bands.

(4) Cloud top temperature observed by MODIS reflects the development of storm cloud bands. The temperature of convective cloud top is lower in the southeast part of the storm but higher in the eye region. The simulated results have similar features as that of the satellite, but with a lower value, indicating the higher cloud top in the simulation. The reflectivity and distribution of ice water in the model correspond well with that retrieved from CloudSat. Strong convection is mostly in the eye wall and clouds extend to the upper level.

(5) In different parts of the storm, the atmosphere below 500 hPa is saturated or weakly supersaturated. Heavy rainfall in the northeast part primarily comes from melting of graupel, auto-conversion of cloud to rain, and collision between raindrops and cloud droplets. Nonetheless, the melting of snow plays an important role in the southwest part to form the relative uniform precipitation.

(6) Downdraft is dominant in the storm center, and the distribution of hydrometeors has a close relationship with updraft. In the north part of the cloud bands, the strongest updraft is in a warm area

below the freezing level, acting as a necessary condition for the formation of abundant precipitation particles. However, in the south part of the storm, the strongest updraft is in the upper cold cloud to favor the genesis and development of ice particles.

REFERENCES:

[1] DUAN Yi-hong. Unusual variation of landfall tropical cyclone behavior and associated physical mechanism[C]//WMO 2nd International Workshop on Tropical Cyclone Landfall Processes (IWTCLP-Ⅱ) extended abstract volume, 2009: 9-12.
[2] DONG Mei-ying, CHEN Lian-shou, ZHENG Pei-jun, et al. Research progress of abrupt intensification of heavy rainfall and super heavy rainfall associated with landfalling tropical cyclones [J]. J. Trop. Meteor., 2009, 25(4): 495-502.
[3] LI Jiang-nan, WANG An-yu, YANG Zhao-li, et al. Advancement in the study of typhoon rainstorm [J]. J. Trop. Meteor., 2003, 19 (suppl.): 152-159.
[4] CHEN Lian-shou, LUO Zhe-xian, LI Ying. Research advances on tropical cyclone landfall process [J]. Acta Meteor. Sinica, 2004, 62(5): 541-549.
[5] ZHU T, ZHANG D L. Numerical simulation of Hurricane Bonnie (1998). Part II: Sensitivity to varying cloud microphysical processes [J]. J. Atmos. Sci., 2006, 63(1): 109-126.
[6] WANG Y. An explicit simulation of tropical cyclones with a triply nested movable mesh primitive equation model: TCM3. Part II: Model refinements and sensitivity to cloud microphysics parameterization [J]. Mon. Wea. Rev., 2002, 130: 3022-3036.
[7] FRANKLIN C N, HOLLAND G J, MAY P T. Sensitivity of tropical cyclone rainbands to ice-phase microphysics [J]. Mon. Wea. Rev., 2005, 133: 2473-2493.
[8] LIU Xiao-bo, ZOU Lan-jun, XIA Li. Analysis on the characteristics and reason of heavy rain and strong wind in Shanghai caused by typhoon Krosa [J]. Meteor. Mon., 2008, 34(12): 72-78.
[9] ZENG Xin-xin, HUANG Xin-qing, TENG Dai-gao. Analysis on torrential rain and super torrential rain in Zhejiang caused by typhoon Krosa [J]. Wea. Fore. Rev., 2009, 1(6): 10-17.
[10] XUE Ji-shan, CHEN De-hui. Scientific design and application of the numerical prediction system GRAPES [M]. Beijing: Science Press, 2008: 137.
[11] CHEN Xiao-min, LIU Qi-jun, ZHANG Jian-cheng. A numerical simulation study on microphysical structure and cloud seeding in cloud system of Qilian Mountain region [J]. Meteor. Mon., 2007, 33(7): 33-43.
[12] DING Zhi-ying, ZHANG Xin-qiang, HE Jin-hai, et al. The study of storm rainfall caused by interaction between the non-zonal high level jet streak and the far distant typhoon [J]. J. Trop. Meteor., 2001, 17(2): 144-152.
[13] STEPHENS G L, et al. The CloudSat mission and the A-train [J]. Bull. Amer. Meteor. Soc., 2002, 83: 1771-1790.
[14] HAYNES J M, STEPHENS G L. Tropical oceanic cloudiness and the incidence of precipitation: Early results from CloudSat [J]. Geophys. Res. Lett., 2007, 34: 1029-1038.
[15] ZHOU Yu-quan, ZHAO Shu-hui. CloudSat satellite and its application in weather and cloud observation [J]. J. Nanjing Inst. Meteor. 2008, 31(5): 603-614.

Citation: HUA Cong and LIU Qi-jun. Numerical simulation of cloud microphysical characteristics of landfall typhoon Krosa. *J. Trop. Meteor.*, 2013, 19(3): 284-296.